

Cite this: DOI: 10.1039/xxxxxxxxxx

Desorption dynamics of RbHe exciplexes off He nanodroplets induced by spin-relaxation

François Coppens,^{a,†} Johannes von Vangerow,^{b,†} Manuel Barranco,^{a,c,d} Nadine Halberstadt,^a Frank Stienkemeier,^b Martí Pi^{c,d}, and Marcel Mudrich^e

Received Date

Accepted Date

DOI: 10.1039/xxxxxxxxxx

www.rsc.org/journalname

Doped He nanodroplets are ideal model systems to study the dynamics of elementary photo-physical processes in heterogeneous nanosystems. Here we present a combined experimental and theoretical investigation of the formation of free RbHe exciplex molecules from laser-excited Rb-doped He nanodroplets. Upon excitation of a droplet-bound Rb atom to the $5p_{3/2}^2\Pi_{3/2}$ -state, a stable RbHe exciplex forms within about 20 ps. Only due to $^2\Pi_{3/2} \rightarrow ^2\Pi_{1/2}$ spin-relaxation does the RbHe exciplex detach from the He droplet surface with a half life of about 700 ps, given by the spin-relaxation time and the coupling of spin and translational degrees of freedom.

1 Introduction

Understanding the photochemistry of condensed phase systems and surfaces is essential in many research areas, such as atmospheric sciences¹ and photocatalysis². However, complex couplings between electronic and motional degrees of freedom of various subunits of the system often present a major challenge^{3–5}. Moreover, the heterogeneity of multi-component solid or liquid systems and experimental difficulties in precisely preparing the sample and reproducing measurements tend to make it hard to unravel specific elementary reactions. In this respect, He nanodroplets doped with single atoms or well-defined complexes are ideal model systems for studying photodynamical processes in the condensed phase, both experimentally and theoretically. Due to their ultralow temperature (0.37 K) and their quantum fluid nature, He nanodroplets have a homogeneous density distribution and dopant particles aggregate into cold clusters mostly inside the droplets^{6,7}. Only alkali metal atoms and small clusters are attached to He droplets in loosely bound dimple-like states at the droplet surface^{8–15}.

While He nanodroplets are extremely inert and weakly-perturbing matrices for spectroscopy of embedded atoms and

molecules in their electronic ground state, a rich photochemical dynamics is initiated upon photoexcitation or photoionization^{16,17}. This includes electronic relaxation^{18–21}, the ejection of the dopant out of the droplet^{22–29}, chemical reactions within the dopant complex^{30–32}, and even among the dopant and the surrounding He^{23,33–42}.

As a general trend, electronically excited dopant atoms and small molecules tend to be ejected out of He droplets either as bare particles or with a few He atoms attached to them^{18,43–45}. In particular, all atomic alkali species promptly desorb off the droplet surface, the only exceptions being Rb and Cs atoms in their lowest excited states^{46,47}. The dynamics of the desorption process has recently been studied at an increasing level of detail^{19,24,26,48}, including time-resolved experiments and simulations^{27,29}. The focus has been on the competing processes of desorption of the dopant induced by laser excitation, and the dopant falling back into the He droplet upon photoionization. The latter occurred at short pump-probe delay times when the distance between the photoion and the droplet was short enough for ion-He attraction to be effective.

The aim of this work is to extend our joint experimental and theoretical study of the photodynamics of Rb-doped He nanodroplets to RbHe exciplexes^{26,29}. The simultaneous effect of pair-wise Rb-He attraction and repulsion of Rb from the He droplet as a whole results in an intricate dynamics, and interpretations have remained somewhat ambiguous with respect to the exciplex formation mechanism and characteristic time scale, as well as the origin of free exciplexes detached from the He droplets^{19,29,33,34,36,37}. In particular the role of relaxation of internal degrees of freedom of the RbHe exciplex in the desorption process has not been explicitly addressed^{49,50}. Here, we discuss in detail the interplay of the RbHe formation dynamics, the

^a Laboratoire des Collisions, Agrégats, Réactivité, IRSAMC, Université Toulouse 3- Paul Sabatier, CNRS UMR 5589, 118 route de Narbonne, F-31062 Toulouse Cedex 09, France

^b Physikalisches Institut, Universität Freiburg, Hermann-Herder-Str. 3, 79104 Freiburg, Germany

^c Institute of Nanoscience and Nanotechnology (IN2UB), Universitat de Barcelona, Diagonal 645, 08028 Barcelona, Spain

^d Departament FQA, Facultat de Física, Universitat de Barcelona. Diagonal 645, 08028 Barcelona, Spain

^e Department of Physics and Astronomy, Aarhus University, Ny Munkegade 120, Aarhus 8000 C, Denmark

[†] F. Coppens and J. von Vangerow contributed equally to this work.

* E-mail: mudrich@phys.au.dk

RbHe desorption off the He droplet surface, and the fall-back of $[\text{RbHe}]^+$ created by photoionization in femtosecond pump-probe experiments^{27,29,34}. We find that electronic spin-relaxation is the main process driving the desorption of RbHe off the He droplet.

This paper is accompanied by animations showing the real-time dynamics of the Rb-He droplet complex for several excited states and for the scenario of time-delayed spin-relaxation. These animations are presented in the supplementary material S1-S4.

2 Methods

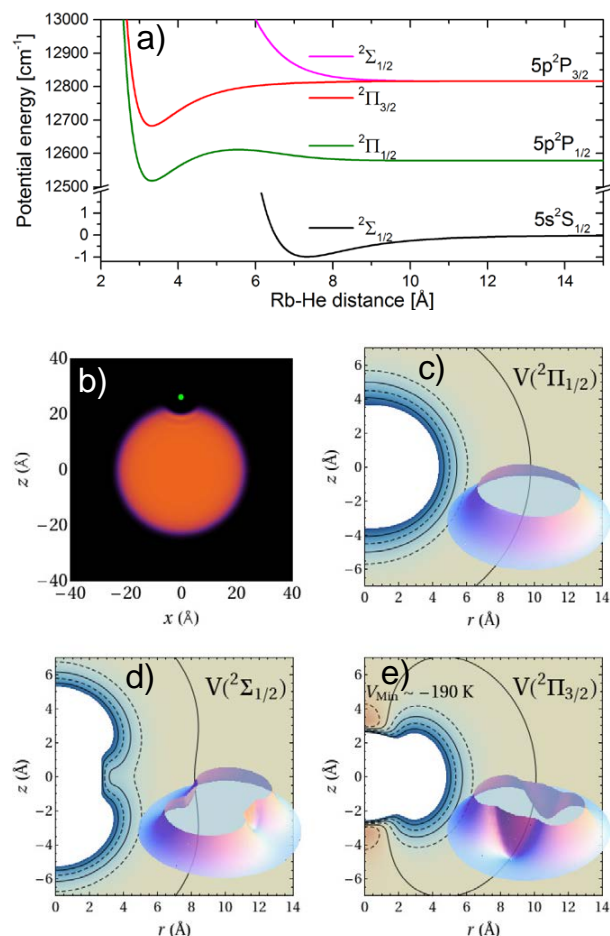


Figure 1 a) Rb-He pair potentials used in this work^{51,52}. The potentials correlating to the Rb excited $5p^2P$ -state are split due to spin-orbit coupling. b) Equilibrium dimple configuration of Rb in the ground state in the x - z -plane (represented by a green dot). Panels c)-e) display the two-dimensional Rb-He potential surfaces in cylindrical coordinates (r , z) corresponding to this configuration, with the Rb atom located at the origin. Regions where the potentials are attractive (repulsive) are represented in pink (blue). The outermost equidensity line corresponds to zero potential. Notice that in panel e) the $5p^2\Pi_{3/2}$ potential presents a deep minimum of about 190 K on the z -axis. The $5p^2\Pi_{1/2}$ and $5p^2\Sigma_{1/2}$ potentials [c) and d)] have shallow attractive minima of about 1 K depth at a distance of ~ 10 Å, not represented in the figure. Reprinted from Int. Rev. Phys. Chem. **36**, 621-707 (2017) with permission from Taylor & Francis Ltd, <http://www.tandfonline.com>.

2.1 Theoretical approach

During the last decade, the density functional theory (DFT) approach has emerged as an accurate and flexible tool to describe the statics and dynamics of doped helium droplets. The DFT activity carried out in this field has been summarized in two reviews^{10,17}. In the following we give the basic details how the method has been applied to the present problem, and refer the reader to Refs.^{17,25} for the details.

In this work, we describe the interaction of a Rb atom with a He droplet composed of $N = 1000$ He atoms. Due to its large mass, Rb is treated as an external field in the statics, and as a classical particle in the dynamics. The impurity-droplet interaction is described in a pairwise approximation, and the ground state of the droplet-impurity system is found by solving the Euler-Lagrange equation

$$\left\{ -\frac{\hbar^2}{2m} \nabla^2 + \frac{\delta \mathcal{E}_c}{\delta \rho} + V_X(|\mathbf{r} - \mathbf{r}_I|) \right\} \Psi_0(\mathbf{r}) = \mu \Psi_0(\mathbf{r}), \quad (1)$$

where $\Psi_0(\mathbf{r}) = \sqrt{\rho(\mathbf{r})}$ is the He effective wave function, with $\rho(\mathbf{r})$ being the atom density; μ is the He chemical potential, and V_X is the Rb-He pair potential⁵¹. The correlation energy density functional \mathcal{E}_c has been taken from Ref.⁵³. The results presented in this work are obtained using the 4He-DFT BCN-TLS computing package⁵⁴. We work in Cartesian coordinates using a space step of 0.4 Å. In the dynamics calculations we use a time step of 0.5 fs.

Once the droplet-equilibrium configuration, shown in Figure 1 b), is determined, the $5p \leftarrow 5s$ absorption spectrum is obtained using the DF sampling method⁵⁵. To this end, the diatomic-in-molecule model is used for the droplet-Rb interaction in the excited $5p^2P$ state⁵⁶. The $5p^2\Sigma$ and $5p^2\Pi$ Rb-He pair potentials, shown in Figure 1 a), are taken from Refs.^{51,52}. The resulting simulated absorption dipole spectrum of the RbHe_{1000} complex, shown in Figure 6 of Ref.¹⁷, is in good agreement with the experiment and previous calculations^{34,57}.

Figs. 1 c)-e) show the direction-dependent potentials (spin-orbit term included) which, within the diatomic-in-molecule approach, enter the dynamics simulations of Rb in the $5p^2P$ -correlated states. In the course of the time evolution of the system, the He atoms have a natural tendency to adapt to these potential surfaces, either going away if the potential is mostly repulsive as in the $\Sigma_{1/2}$ -state [Figure 1 d)], or to evolve to a bound RbHe exciplex configuration in the $\Pi_{3/2}$ -state [e)] featuring local minima at $(r=0, z=\pm 3.5)$ Å. In the $\Pi_{1/2}$ -state [c)], one may also expect the formation of RbHe exciplexes given the potential minimum in the RbHe pair potential around 3.2 Å [a)]. However, RbHe formation is hampered by a potential barrier which cannot be overcome at the low temperature of the He droplet^{34,58}.

2.2 Experimental setup

The setup used for the present experiments has been described previously^{26,27}. Briefly, a beam of He droplets with an average diameter of 10 nm is produced by continuously expanding pressurized He (50 bar) out of a cold nozzle (diameter 5 μm , temperature 17 K). The He droplets are doped with one Rb atom on

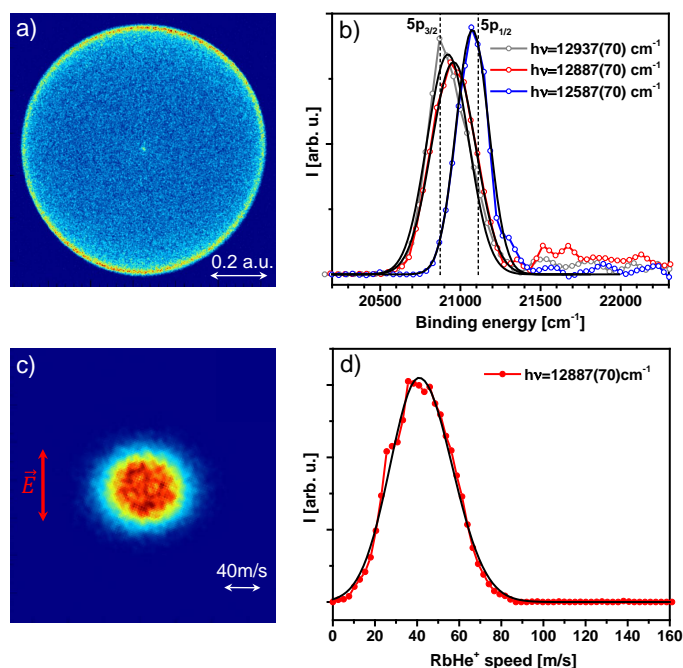


Figure 2 Raw velocity-map images of photoelectrons a) and of $[\text{RbHe}]^+$ photoions c) recorded at $\lambda = 776 \text{ nm}$ (12887 cm^{-1}) for a long pump-probe delay time of 2 ns. The red vertical arrow indicates the laser polarization. b) Electron binding energy spectra inferred from the image shown in a), from an image recorded at $\lambda = 773 \text{ nm}$ (12937 cm^{-1}), and from an image at $\lambda = 794 \text{ nm}$ (12587 cm^{-1}). d) $[\text{RbHe}]^+$ photoion speed distribution inferred from c).

average by pickup of Rb atoms inside a heated vapor cell (length 1 cm, temperature 85°C).

An amplified Ti:Sa laser system generates pulses of 100 fs duration at a repetition rate of 5 kHz. The center wavelength is tunable in the near infrared (NIR) region. The FWHM of the spectral laser profile is 140 cm^{-1} . Light in the visible range (VIS) is generated by frequency doubling. The pulses are split and separated in time in a Mach-Zehnder type interferometer. The droplet-perturbed Rb 5p states are probed by a two-color NIR+VIS pump-probe resonant photoionization scheme. The NIR pulses are strongly attenuated to avoid the excitation of higher lying states by multi-photon processes. The polarizations of the two laser pulses are parallel to one another and parallel to the detector surface.

Photoions and photoelectrons are detected by a velocity-map imaging (VMI) spectrometer operated in single-particle detection mode^{19,26,59,60}. Mass-selected ion VMIs are recorded by time-gating the imaging detector according to the specific flight times of either Rb^+ or $[\text{RbHe}]^+$ ions. One VMI is recorded for each value of the pump-probe delay time. Both Rb^+ ion images and electron images contain background contributions from resonant ionization of free Rb atoms effusing out of the doping cell. In order to efficiently subtract these contributions, background images are recorded at each pump-probe delay using a chopper that periodically interrupts the He droplet beam at a frequency of 15 Hz. The acquired background and signal+background images are inverse Abel transformed to infer the full three-dimensional velocity

distributions^{61,62}. The resulting spectra obtained from angular integration are normalized to the number of counts and subtracted from each other, where we exploit the additivity of the inverse Abel transformation⁶³.

3 Time-resolved imaging spectroscopy

Typical experimental total electron and $[\text{RbHe}]^+$ ion VMIs recorded at a center wavelength of the pump laser pulse $\lambda = 776 \text{ nm}$ (12887 cm^{-1}) and a pump-probe delay of 2 ns are shown in Figure 2 a) and c), respectively. The corresponding electron binding energy distribution and ion speed distribution inferred from these images are presented in Figure 2 b) and d), respectively. In addition, Figure 2 b) contains photoelectron spectra measured at $\lambda = 773 \text{ nm}$ (12937 cm^{-1}) and at $\lambda = 794 \text{ nm}$ (12587 cm^{-1}). Note that the photoelectron spectra in Figure 2 b) are rescaled in terms of electron binding energies $E_b = h\nu_2 - T_e$, where $h\nu_2 = 2hc/\lambda$ denotes the photon energy of the ionizing laser pulse and T_e is the measured electron kinetic energy. The dashed vertical lines represent E_b for free Rb atoms in their $5p_{1/2}$ and $5p_{3/2}$ -states.

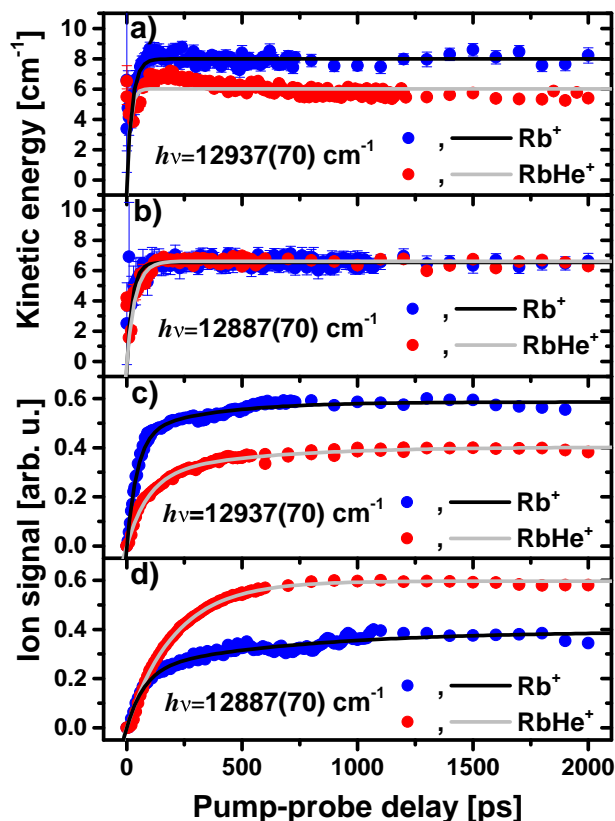


Figure 3 Rb^+ and $[\text{RbHe}]^+$ ion kinetic energies [a) and b)] and signal yields [c) and d)] recorded at laser wavelengths $\lambda = 773 \text{ nm}$ [12937 cm^{-1} , a) and c)] and $\lambda = 776 \text{ nm}$ [12887 cm^{-1} , b) and d)]. The smooth gray and black lines are fit curves (see text for details).

3.1 Photoion imaging

The $[\text{RbHe}]^+$ ion distribution [Figure 2 c)] is a round spot with a flat intensity distribution and a slight elongation in x -direction

(perpendicular to the laser polarization). The corresponding speed distribution [Figure 2 d)] is broad and nearly symmetric. The black line depicts a skewed Gaussian distribution fitted to the data⁶⁴. This fit is applied repeatedly to each speed distribution measured at various pump-probe delays in order to trace the evolution of the most probable kinetic energy, see Figure 3 a) and b). The yields of ions, shown in Figure 3 c) and d), are obtained by summing over ion counts contained in each image. Blue and red symbols show the results for Rb^+ and $[\text{RbHe}]^+$ ions, respectively. Both kinetic energies and ion yields monotonously increase within 50-500 ps, with a slight overshoot at $\lambda = 773$ nm (12937 cm^{-1}) [Figure 3 a)]. This increase results from the competing processes of desorption of the excited neutral Rb and RbHe species, and falling back of the Rb^+ and $[\text{RbHe}]^+$ photoions into the He droplet due to attractive Rb^+ -He interactions, as discussed in Refs.^{27,29}. By comparing the experimental data with TD-DFT simulations, we concluded that the 5p-correlated states of Rb and RbHe desorb off He droplets not purely impulsively, but in a more complex evaporation-like process²⁹. The overshoot of speeds in Figure 3 a) is likely due to weak long-range attractive forces acting between the desorbing Rb and RbHe and the He droplet surface, which slightly slow down the relative motion in the later stage of desorption.

The data in Figure 3 a) are measured at $\lambda = 773$ nm (12937 cm^{-1}), which corresponds to the excitation of the RbHe complex into the $5p\Sigma_{1/2}$ -state, with some contribution of the $5p\Pi_{3/2}$ -state due to overlapping absorption bands and due to the broad spectral profile of the laser^{9,34,65}. The $5p\Sigma_{1/2}$ -state is the most repulsive one out of the three states studied here. Accordingly, the asymptotic most probable speed of Rb^+ reached at long delays is comparatively high, $\hat{v} = 85\text{ m/s}$, corresponding to a kinetic energy of 8 cm^{-1} , whereas for $[\text{RbHe}]^+$ we find $\hat{v} = 40\text{ m/s}$ (5.8 cm^{-1}). Since the diatomic $5p\Sigma_{1/2}$ RbHe potential is purely repulsive [Figure 1 a)], this component of the excited population results in the desorption of neat Rb atoms. Accordingly, the yield of detected Rb^+ ions exceeds that of $[\text{RbHe}]^+$ ions by about a factor 1.5.

At $\lambda = 776$ nm (12887 cm^{-1}), a higher contribution of the $5p\Pi_{3/2}$ -state is excited, which efficiently forms RbHe exciplexes³⁴. Thus, the yield of $[\text{RbHe}]^+$ ions is higher than that of Rb^+ by a factor 1.5. The Rb^+ and $[\text{RbHe}]^+$ asymptotic most probable speed is $\hat{v} = 42\text{ m/s}$ (6.3 cm^{-1}), close to that of $[\text{RbHe}]^+$ at $\lambda = 773$ nm (12937 cm^{-1}). At $\lambda = 794$ nm (12595 cm^{-1}), the $5p\Pi_{1/2}$ -state of the Rb-He droplet complex is excited (not shown), and no $[\text{RbHe}]^+$ ions are detected. Therefore we have recorded only Rb^+ ion images at that wavelength²⁹. Here, the Rb^+ asymptotic most probable speed is lowest, $\hat{v} = 38\text{ m/s}$ (5.1 cm^{-1}), because dopant-He repulsion is weak.

The transient kinetic energies measured at all laser wavelengths rise within a delay time of about 50 ps. The characteristic energy rise time (to half value), τ_E^i , and the asymptotic ion kinetic energy E_∞^i , are determined by fitting the data with an exponential function

$$E^i(t) = E_\infty^i \cdot \left(1 - \exp[-\ln 2 \cdot t / \tau_E^i]\right). \quad (2)$$

The resulting fit parameters are summarized in table 1.

The ion yields increase with pump-probe delay slightly more slowly than the ion kinetic energies, where the Rb^+ ion signal rises faster than the $[\text{RbHe}]^+$ ion signal at short delays. The initial fast rise of the Rb^+ ion yield flattens out at delays around 100 ps and continues to rise slightly up to about 2 ns. The $[\text{RbHe}]^+$ ion yields show a similar initial fast rise followed by a more pronounced slow increase that levels off somewhat earlier. Therefore, for fitting the Rb^+ and $[\text{RbHe}]^+$ ion yield data we use a biexponential function,

$$I(t) = A_1^i \cdot \left(1 - \exp[-\ln 2 \cdot t / \tau_1^i]\right) + A_2^i \cdot \left(1 - \exp[-\ln 2 \cdot t / \tau_2^i]\right), \quad (3)$$

where (A_1^i, τ_1^i) and (A_2^i, τ_2^i) parametrize the fast and the slow signal rise, respectively.

While neither the Rb^+ and $[\text{RbHe}]^+$ asymptotic energies E_∞^i , nor the energy rise times τ_E^i depend much on λ , the rise times of ion yields of RbHe^+ , τ_1^i , clearly decrease monotonically with decreasing λ (increasing photon energy) by a factor 6, ranging from 186 ps at $\lambda = 780$ nm (12821 cm^{-1}) to 32 ps at $\lambda = 773$ nm (12937 cm^{-1}). The trend that the dynamics proceeds faster with decreasing λ (increasing photon energy) is partly due to the increasingly repulsive dopant-He interaction and agrees with our previous findings^{27,29}. However, the observation that the ion yields rise more slowly than the ion kinetic energies cannot be understood with the concept of impulsive desorption and fall-back. In that model, ion kinetic energies should be affected by ion-He attraction up to long delay times exceeding the fall-back time. Note that in previous experiments on the Rb 6p-state, where desorption proceeded impulsively, ion energies indeed increased more slowly than ion yields²⁹. Therefore we take our current finding ($\tau_1^i, \tau_2^i > \tau_E^i$) as a further indication for a non-impulsive, evaporation-like desorption mechanism.

Furthermore, from our analysis of the VMIs we obtain information about the anisotropy of the ion angular distribution, characterized by the parameter β ⁶⁶. For $[\text{RbHe}]^+$ at long delay times we find $\beta = -0.39(1)$ when a higher contribution of the $\Pi_{3/2}$ -state is excited at $\lambda = 776$ nm (12887 cm^{-1}). At $\lambda = 773$ nm (mainly $\Sigma_{1/2}$ -excitation), the anisotropy becomes slightly positive, $\beta = 0.13(1)$. The corresponding values for the Rb^+ ion distributions are $\beta = -0.16(1)$ and $\beta = 0.17(1)$, respectively. While the signs of the β -values are in accordance with the symmetries of the pseudo-diatomic states (ideal perpendicular $\Sigma \rightarrow \Pi$ -transition in a diatomic implies $\beta = -1$, parallel $\Sigma \rightarrow \Sigma$ -transition implies $\beta = 2$), the absolute values are much smaller. On the one hand, this is due to the mixing of excited $\Sigma_{1/2}$ and $\Pi_{3/2}$ -states. On the other hand, the desorption process is more complex than direct dissociation of a diatomic molecule. We recall that the β -values came much closer to the ideal values in the case of excitation of Rb to the high-lying 6p-correlated states, where desorption proceeded more impulsively^{19,26,29}.

We mention that in earlier pump-probe experiments, significantly different Rb^+ and $[\text{RbHe}]^+$ ion yield curves were measured³⁶. However, in those experiments, NIR light emitted directly from a mode-locked titanium:sapphire laser was used at

λ [nm]	State	Ion	E_{∞}^i [1/cm]	τ_E^i [ps]	A_1^i	τ_1^i [ps]	A_2^i	τ_2^i [ps]	β
773	$\Sigma_{1/2}/\Pi_{3/2}$	Rb ⁺	8.0(1)	17(1)	0.45(2)	32(1)	0.14(2)	234(33)	0.17(1)
		[RbHe] ⁺	6.0(1)	10(2)	0.17(2)	41(6)	0.22(2)	178(17)	0.13(1)
776	$\Pi_{3/2}/\Sigma_{1/2}$	Rb ⁺	6.5(3)	17(1)	0.24(2)	53(5)	0.16(2)	490(104)	-0.16(1)
		[RbHe] ⁺	6.6(3)	26(1)	0.60(1)	143(2)	0.00(1)	-	-0.39(1)
780	$\Pi_{3/2}$	[RbHe] ⁺	6.3(1)	24(2)	0.95(1)	186(1)	0.00(1)	-	0.35(1)

Table 1 Time constants and energies inferred from pump-probe measurements of Rb⁺ and [RbHe]⁺ ion yields at the 5p $\Sigma_{1/2}$ and 5p $\Pi_{3/2}$ -states of the Rb-He droplet complex, obtained from fits with equations (2) and (3), see Figure 3.

a pulse repetition rate of 80 MHz. Therefore, a large fraction of the ion signals actually stemmed from Rb and RbHe that had been desorbed off the droplets by preceding pulse pairs. Thus, the observed pump-probe transients may have reflected the internal dynamics of free RbHe instead of the dynamics of the Rb-He droplet interaction. Besides, near-resonant two-photon excitation of higher lying states correlating to the Rb 5d-level were probably involved in the observed dynamics. This raises some doubts as to the conclusions of those previous experiments in terms of exciplex formation times^{29,36}. Further studies are needed to clarify this issue.

From the overall resemblance of the [RbHe]⁺ and Rb⁺ kinetic energy curves and ion yields in the present study one is tempted to conclude that RbHe exciplex formation is fast and desorption of RbHe off the He droplet surface proceeds essentially in the same way as for neat Rb atoms. However, the more pronounced biexponential rise of [RbHe]⁺ ion yields, as well as complementary delay-dependent photoelectron measurements, and numerical simulations presented in the following sections will show that the desorption dynamics of RbHe exciplexes actually is more intricate than that of Rb atoms.

3.2 Photoelectron imaging

The photoelectron spectra recorded at the three characteristic laser wavelengths λ [Figure 2 b)] exhibit pronounced peaks around the Rb 5p $_{1/2}$ and 5p $_{3/2}$ atomic binding energies, $E_{5p1/2}$ and $E_{5p3/2}$, respectively. Both the peak position and the peak width significantly vary with λ , as inferred from fits to the data with a Gaussian function, depicted as smooth lines. The resulting peak positions relative to $E_{5p1/2}$ and $E_{5p3/2}$ are plotted in Figure 4 a), b), respectively. Figure 4 c) shows the Gaussian peak widths σ . For reference, the open symbols represent the peak positions measured for the Rb atomic background. The scatter of data points around the literature value (grey horizontal line) indicates the level of precision of our measurements.

The excess energies for the 5p $\Sigma_{1/2}$ and 5p $\Pi_{3/2}$ -states, $E_b - E_{5p1/2,5p3/2}$ shown in Figure 4 b), exhibit a fast decay (E_1^e , τ_1^e) above and a slow decay (E_2^e , τ_2^e) below $E_{5p3/2}$ (horizontal line at $y = 0$). Therefore, these data are fitted with a biexponential decay function

$$E^e(t) = E_1^e \cdot \exp(-\ln 2 \cdot t/\tau_1^e) + E_2^e \cdot \exp(-\ln 2 \cdot t/\tau_2^e) + E_{\infty}^e. \quad (4)$$

Here, E_{∞}^e denotes the asymptotic energy value at long delay times. When exciting the 5p $\Pi_{1/2}$ -state at $\lambda = 794$ nm (12594 cm⁻¹),

the transient droplet correlated peak position remains constant within the experimental scatter. Therefore, merely the mean value E_1^e is determined. The resulting energies and time constants are summarized in table 2. The increasing peak widths in the cases of $\lambda = 773$ (12937 cm⁻¹) and 776 nm (12887 cm⁻¹) are fitted by the simple exponential function given by Eq. (2).

The fact that the droplet-related photoelectron energy E_1^e for the $\Pi_{1/2}$ -state is constant but shifted with respect to the atomic value indicates that most of the Rb atoms remain attached to the droplet surface upon electronic excitation, in accordance with previous studies^{46,67}. Thus, the slowly rising Rb⁺-ion signal measured at that wavelength, indicative for excited Rb desorption, reflects only a small fraction of Rb atoms, most of which actually remain bound to the droplets. The measured up-shift of electron energy of $E_1^e = 33(2)$ cm⁻¹ is attributed to a lowering of the ionization threshold induced by the He environment. This value is in reasonable agreement with previous measurements, where the ionization threshold was found to be lowered by 50(10) cm⁻¹ at comparable conditions⁶⁷.

The similar dynamics of electron energies and ion yields for the $\Sigma_{1/2}$ and $\Pi_{3/2}$ -states, a biexponential evolution with a fast component (tens of ps) and a slow component (hundreds of ps), are taken as a confirmation that two distinct relaxation processes occur simultaneously. The fast process – prompt desorption of excited Rb off the He droplet – is associated mainly with the $\Sigma_{1/2}$ -component of the excited state, whereas the $\Pi_{3/2}$ -component undergoes slow relaxation. The latter will be discussed in the following sections. Deviations of the time constants τ_1^i vs. τ_1^e , and τ_2^i vs. τ_2^e , are mainly due to the different nature of the observables. Both ion yields and speeds are affected by the dynamics occurring *after* the probe-ionization, whereas electron spectra probe the electronic state (affected by the He configuration around the Rb) *at the moment* of ionization. In particular, ion signals provide information only about that fraction of ions that eventually detach from the He droplets, whereas electron signals are measured for all photoionization events, including those where the ion falls back into the droplet; in this respect the electron spectra are the better probes of the full dynamics, with the restriction that we cannot distinguish between the final products (Rb, RbHe, and Rb attached to a He droplet).

We mention that at $\lambda = 776$ nm (12887 cm⁻¹, $\Pi_{3/2}$ -state), an extended low intensity distribution is present in the spectrum of Figure 2 b) at higher electron binding energies $\geq 21,500$ cm⁻¹ (lower electron kinetic energies). We attribute this component to elastic scattering of photoelectrons with He atoms as they prop-

λ [nm]	State	E_1^e [1/cm]	τ_1^e [ps]	E_2^e [1/cm]	τ_2^e [ps]	E_∞^e [1/cm]
773	$\Sigma_{1/2}/\Pi_{3/2}$	32(2)	15(2)	63(4)	683(130)	-53(5)
776	$\Pi_{3/2}/\Sigma_{1/2}$	36(2)	13(2)	110(4)	709(70)	-96(5)
794	$\Pi_{1/2}$	33(2)	-	-	-	-

Table 2 Time constants and energies inferred from fits of equation (4) to the transient photoelectron energies (Figure 4).

agate through the He droplet. Low-energy features in photoelectron spectra due to electron-He scattering have been observed before, in particular when using one-photon ionization^{68–71}. The fact that this feature is most pronounced for the $\Pi_{3/2}$ -excitation may be related to the more abundant formation of RbHe exciplexes which enhances the electron-He scattering probability.

4 TD-DFT dynamics simulation

Time-dependent density functional theory (TD-DFT) simulations are carried out as thoroughly described in Refs.^{17,25}. Starting with the Rb-droplet equilibrium configuration, the dynamics is initiated by a “vertical DFT transition” into the excited state. This is realized by suddenly switching from the potential energy surface of the Rb-He droplet ground state to that of the Rb-He excited state. The subsequent evolution of the system can be followed in real-time, as illustrated by the series of snapshots of the He density distribution (red area) and the position of the Rb atom (green and magenta dots) in Figure 5. **The animated version of this evolution is shown in the Video S4 in the supplementary material.** Here, excitation of the $5p\Pi_{3/2}$ -state at $t = 0$ is followed by relaxation to the $5p\Pi_{1/2}$ -state at $t = 60$ ps. This time has been chosen rather arbitrarily; the only constraint is that it should be large enough to allow the exciplex around the $5p\Pi_{3/2}$ -state to fully develop, see Figure 7 below.

4.1 Direct ejection of bare Rb atoms from the $^2\Sigma_{1/2}$ and $^2\Pi_{1/2}$ -states

From these data we now infer the relevant quantities to compare with the experimental results, such as the kinetic energy of the Rb atom relative to the droplet, the occurrence of He density attached to Rb which we identify with the formation of an exciplex, and the transient interaction energy of the neutral and ionized Rb atom with the surrounding He. The latter is related to the kinetic energy of a photoelectron created in a time-delayed photoionization process.

Figure 6 collects our results for the dynamics of the Rb atom excited to the droplet-perturbed states correlating to the atomic $5p$ -state. For the $\Sigma_{1/2}$ and $\Pi_{1/2}$ -states, the velocities (dashed lines) and kinetic energies (solid lines) feature a rapid increase to reach a maximum at time $t = 2$ –5 ps after excitation, followed by a drop due to long-range attractive forces acting on the desorbing Rb atom. The asymptotic values are reached for $t > 50$ ps. When exciting the $\Pi_{3/2}$ -state, the Rb-velocity features a damped oscillation around zero indicating that the Rb atom remains bound to the He droplet surface. The following conclusions can be drawn from these results:

(i) Rb excited to the $5p\Sigma_{1/2}$ -state detaches from the droplet

reaching an asymptotic kinetic energy of 13 cm^{-1} . This value deviates from the experimental one (8.0 cm^{-1}) due to contributions of $\Pi_{3/2}$ -excitation to the experimental signal. Despite of the shallow local minima in the corresponding Rb-He droplet potential surface [1 c)], no binding of He density to the departing Rb atom occurs. This finding is in accordance with experiments^{19,34,36}, where mostly free Rb atoms were detected following excitation at wavelengths $\lambda < 774\text{ nm}$ ($> 12929\text{ cm}^{-1}$). **The full evolution of the excited Rb-He nanodroplet complex is shown in the Video S1 in the supplementary material.**

(ii) Rb excited to the $5p\Pi_{1/2}$ -state also detaches from the He droplet, but the asymptotic kinetic energy is much lower, 2.8 cm^{-1} . **For this case, the evolution is shown in the Video S2 in the supplementary material.** This value of the Rb kinetic energy again deviates from the experimental one (5.1 cm^{-1}), but the trend that desorption of the less repulsive $\Pi_{1/2}$ -state yields a lower energy than for the $\Sigma_{1/2}$ -state is well reproduced. The potential well at short distance $\sim 3\text{ \AA}$ would in principle support a stable RbHe exciplex. However, at the low temperature of the He droplet, exciplex formation is hindered by a potential barrier located at $\sim 5\text{ \AA}$, between the well and the range where the $5p\Pi_{1/2}$ -state is populated by excitation from the $5s\Sigma_{1/2}$ -ground state (7 \AA)^{33,34,58}.

We recall that in previous experiments using narrow-band excitation of the low energy edge of the $\Pi_{1/2}$ -resonance, it was observed that Rb and Cs dopants remained attached to the He droplet surface⁴⁶. However, our simulations correspond to the excitation at the peak of the resonance, where free Rb atoms are also observed in the experiment. Thus, our simulations are not in conflict with the experimental findings. Note that Quantum Monte Carlo (QMC) calculations carried out for this state⁷² yielded a weakly bound Rb in a shallow dimple. Had we carried out a *static* DFT relaxation, we would also have found a bound structure, due to the shallow minimum on the Rb-He droplet potential surface. However, in the dynamical TD-DFT simulation this minimum is too shallow to retain the departing Rb atom.

(iii) In our simulation we find that Rb excited to the $5p\Pi_{3/2}$ -state remains bound to the He droplet surface where it forms a RbHe exciplex **(see Video S3 in the supplementary material)**. Figure 1 shows two deep barrierless potential wells at a Rb-He distance of about 3 \AA . In the course of the dynamics, the Rb atom is drawn to the well close to the droplet surface, develops a RbHe exciplex that remains bound to it, and oscillates around an equilibrium position of $\sim 3\text{ \AA}$ above the static equilibrium position at the dimple as shown in Figure 6. This result is in full agreement with static QMC calculations by Leino et al.⁴⁹. Note that our simulations do not provide any indication that the vibrational motion

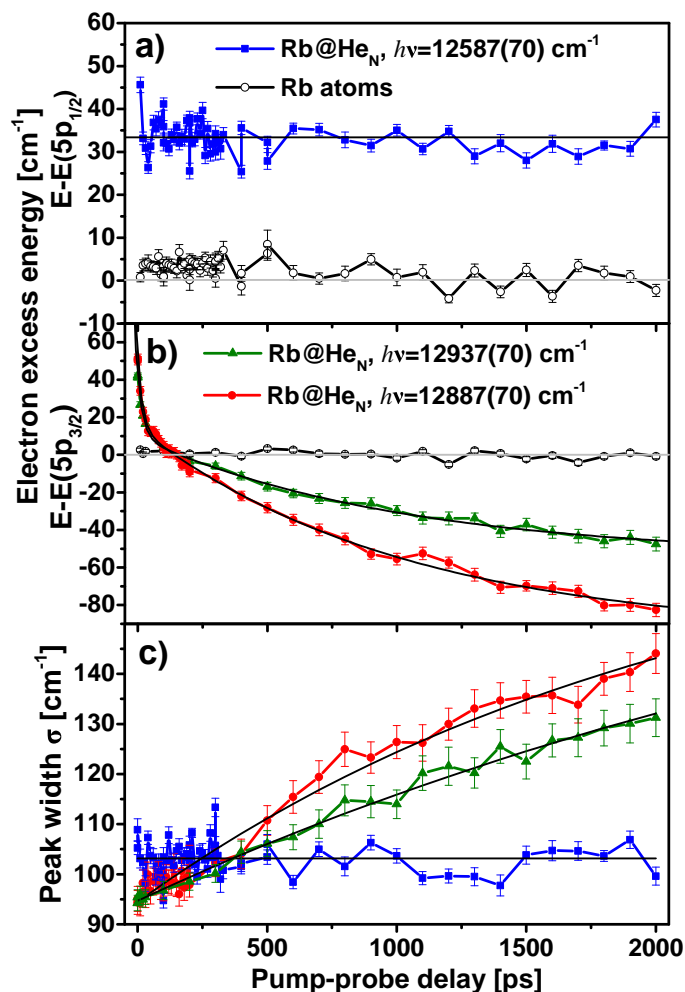


Figure 4 Photoelectron energies as a function of pump-probe delay (filled circles) recorded at laser wavelengths $\lambda = 794$ nm (12594 cm^{-1} , $5p\Pi_{1/2}$) (a), $\lambda = 773$ nm (12937 cm^{-1} , $5p\Pi_{1/2}$), and $\lambda = 776$ nm (12887 cm^{-1} , $5p\Pi_{3/2}$) (b). Open circles indicate the electron energies measured for atomic Rb background signal. The widths of electron distributions are depicted in (c).

of the RbHe exciplex structure leads to its desorption from the He droplet.

The dynamics of the exciplex formation process can be quantitatively represented by integrating over the He density within a spherical inclusion volume with radius r_{incl} around Rb. The result is shown in Figure 7. Thus, for $r_{\text{incl}} = 5.7$ Å, which contains the entire localized He density at the Rb atom without including He density of the remaining droplet, we find a rise to 75 % of the final value at $t = 20$ ps. For $t > 60$ ps the He number density stabilizes close to 1, indicating the full evolution of a RbHe exciplex containing 1 He atom. This result is in good agreement with the formation time estimated using the tunneling model by Reho et al.³³ using model parameters inferred from the previous fs-ps pump-probe measurements (42 ps)⁵⁰.

The finding that the RbHe exciplex remains attached to the He droplet is in apparent contradiction to experiments where the ejection of free Rb and RbHe was clearly observed^{19,34,36}. Therefore, an additional mechanism must be active that induces the

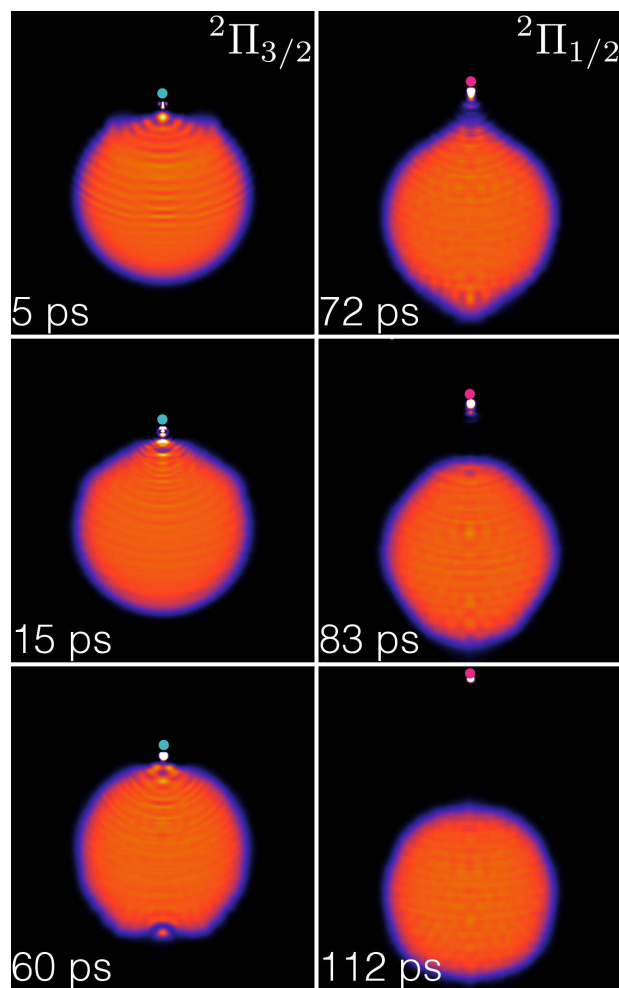


Figure 5 Snapshots of the He density during the evolution of the excited RbHe₁₀₀₀ complex for $\eta = 15\%$, $\Delta t = 60$ ps. The green dot represents the Rb atom excited into the $5p\Pi_{3/2}$ -state; the magenta dot is the Rb atom after suddenly relaxing to the $5p\Pi_{1/2}$ -state. The white spot accompanying the green or magenta dot representing the Rb atom depicts the He density carried away with it.

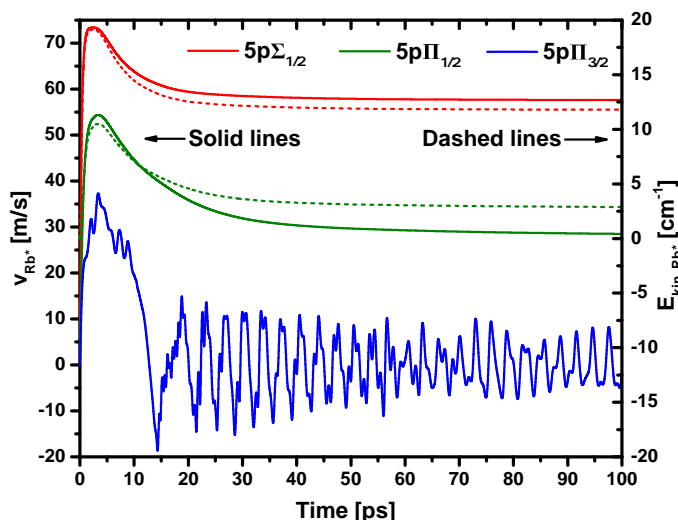


Figure 6 Velocity (solid lines, left scale) and kinetic energy (dashed lines, right scale) of the Rb atom excited to the 5p-state as a function of time. The kinetic energy of the 5pΠ_{3/2}-state is not given as this state remains bound to the droplet.

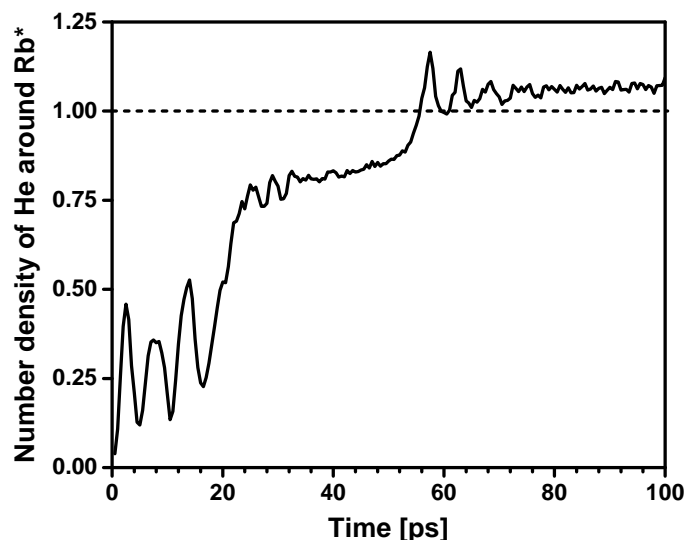


Figure 7 Simulated time evolution of the integrated He density within an inclusion volume of radius $r_{incl} = 5.7$ Å around the Rb atom excited to the 5pΠ_{3/2}-state.

η (%)	v_{∞} (m/s)	Kin. energy (cm ⁻¹)
5	bound	–
10	13.4	0.64
12.5	43.0	6.6
15	62.4	13.9
20	80.4	23.0

Table 3 Asymptotic velocity and kinetic energy of the ejected RbHe exciplex for various values of the fraction η of the 5pΠ_{3/2,1/2}-energy spacing of 165 cm⁻¹, which is converted into kinetic energy of Rb by relaxation from the 5pΠ_{3/2} into the 5pΠ_{1/2}-state. The calculations are carried out at a delay time $\Delta t = 60$ ps between photo-excitation and non-radiative de-excitation of the Rb atom.

desorption of the RbHe molecule off the He droplet surface.

4.2 RbHe exciplex formation around the 5p²Π_{1/2}-state: non-radiative relaxation from the 5p²Π_{3/2}-state

In the gas phase, a RbHe exciplex can form in the 5pΠ_{1/2}-state if enough kinetic energy is provided by collisions such that the Rb can overcome the potential barrier⁵⁸. Alternatively, collisions of a RbHe formed in the 5pΠ_{3/2}-state with another atom or complex might induce relaxation into a RbHe electronic state correlating to the Rb 5p_{1/2}-state. In this case the barrier is circumvented by the relaxation process, as the potential wells for the two states Π_{3/2} and Π_{1/2} are at similar Rb-He distances. In the condensed (droplet) phase at 0.4 K temperature, none of these mechanisms are active to explain the formation of RbHe 5p²Π_{1/2} exciplexes and their potential ejection.

However, Figure 1 a) indicates another possible mechanism: Non-radiative de-excitation from the 5pΠ_{3/2} to the 5pΠ_{1/2}-state accompanied by transfer of energy into the relative motion of the Rb atom away from the He droplet. Notice from the figure that the minimum of the 5pΠ_{3/2}-potential is at ~ 12683 cm⁻¹, and that of the 5pΠ_{1/2}-potential is at ~ 12518 cm⁻¹; the value of this potential at the barrier is 12611 cm⁻¹. Thus, non-radiative de-excitation of the Rb atom may add to its original kinetic energy a fraction of this 165 cm⁻¹ difference energy. Consequently, the RbHe exciplex will be ejected in the 5pΠ_{1/2}-state, and not in the 5pΠ_{3/2}-state that was originally photo-excited. Non-radiative electronic relaxation induced by the He droplet has been observed for a number of metal atoms^{18–21,41,44,73}. In particular, previous measurements of the dispersed fluorescence emitted upon excitation of Rb into the 5pΠ_{3/2}-state of the Rb-He droplet complex have evidenced large populations of free Rb atoms in the 5pΠ_{1/2}-state³⁴. Efficient spin-relaxation of 5pΠ_{3/2}-excited Rb atoms can be rationalized by the large cross section for mixing of fine structure states in collisions of alkali metal atoms with He⁷⁴. For low-temperature Rb-He collisions, the fine structure relaxation rate was found to be enhanced by the transient formation of a RbHe exciplex by orders of magnitude compared to binary Rb-He collisions⁵⁸.

Here, we explore this scenario within TD-DFT. Starting from Rb in the 5pΠ_{3/2}-state, we induce a “vertical DFT transition” by suddenly switching potential energy surfaces from 5pΠ_{3/2} to 5pΠ_{1/2}, imparting to the Rb a kinetic energy corresponding to a fraction

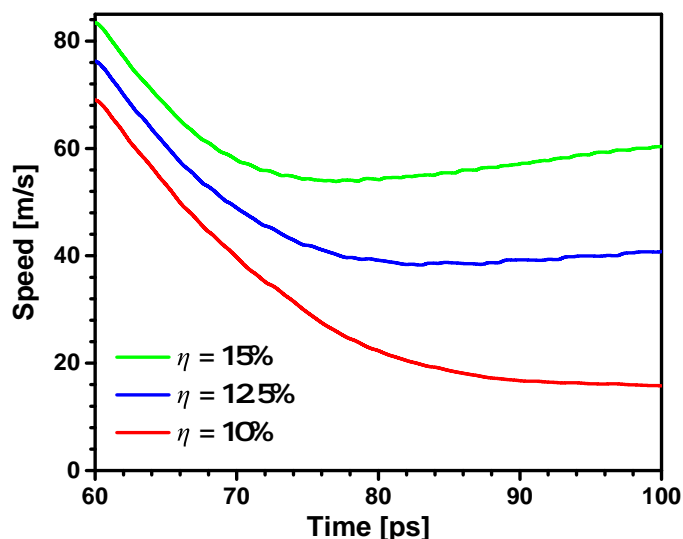


Figure 8 Velocity of the excited Rb atom with attached He density as a function of time after $5p\Pi_{3/2} \rightarrow 5p\Pi_{1/2}$ relaxation at $\Delta t = 60$ ps for various values of the energy conversion factor η .

η of the available non-radiative de-excitation energy. The time Δt elapsing between the vertical excitation and de-excitation has to be chosen as well; this time influences the degree of RbHe $5p\Pi_{3/2}$ exciplex formation which, as we have seen, may require some tens of ps. The actual value of these inputs cannot be determined by the model itself.

In the following, we present results obtained from simulations using as input parameters the delay before relaxation $\Delta t = 60$ ps, and several values of η . As shown in Figure 6 (see also the bottom left panel of Figure 5), this –arbitrary– time is sufficient to allow for a full development of the $5p\Pi_{3/2}$ RbHe exciplex and to bring it to a rather stationary configuration.

The snapshots in Figure 5 and the corresponding animation (Video S4 in the supplementary material) illustrate the evolution following the $5s\Sigma_{1/2} \rightarrow 5p\Pi_{3/2} \rightarrow 5p\Pi_{1/2}$ process for $\eta = 15\%$, $\Delta t = 60$ ps. Thus, upon sudden relaxation to the $5p\Pi_{1/2}$ -state, the RbHe structure promptly detaches from the remaining He droplet. The velocity of the Rb atom as a function of time is depicted in Figure 8 for this and other values of η . Clearly, as the fraction of relaxation energy converted to Rb kinetic energy is increased from 10% to 15%, the initial speed, and even more so, the asymptotic value for long evolution times rises significantly. Table 3 collects the results obtained for various values of η . It can be seen that a fairly small $\eta \geq 10\%$ is enough to induce the ejection of the RbHe complex. For a value $\eta = 12.5\%$, the asymptotic value of the RbHe velocity matches best the experimental one measured for maximum $5p\Pi_{3/2}$ -excitation at $\lambda = 776$ nm (12887 cm^{-1}).

When assuming that the relaxation-induced RbHe desorption proceeds as an impulsive dissociation reaction, the conversion factor η can be related to an effective mass of the He droplet, m_{eff} ²⁴. From $\eta = 12.5\%$ we obtain $m_{eff} = 12.7$ amu, which corresponds to about 3 He atoms effectively interacting with the excited RbHe. This value is significantly less than what was found

for the prompt desorption of Rb and RbHe upon excitation of the Rb 6s and 6p-correlated states^{19,26}. This is no surprise, though, since the orbital overlap between the excited RbHe and the He droplet is smaller than for the higher excited and more extended 6s and 6p-states. Besides, the effective mass model is not strictly valid in the present situation, since it neglects the internal degrees of freedom of RbHe which is taken as one fixed subunit.

Now that we have established the RbHe formation and desorption mechanisms, we can take our comparative study one step further and compute from the simulation results the electron binding energies to compare with the experimental photoelectron spectra. For this, we evaluate the interaction energy of the excited Rb atom and of the Rb^+ ion with the droplet by calculating, respectively,

$$U^*(t) = \int d\mathbf{r} \mathcal{V}_{\text{He-Rb}^*}(|\mathbf{r} - \mathbf{r}_{\text{Rb}^*}|) \rho(\mathbf{r}, t) \quad (5)$$

and

$$U^+(t) = \int d\mathbf{r} \mathcal{V}_{\text{He-Rb}^+}(|\mathbf{r} - \mathbf{r}_{\text{Rb}^+}|) \rho(\mathbf{r}, t). \quad (6)$$

Here the He-Rb⁺ pair potential $\mathcal{V}_{\text{He-Rb}^+}$ is taken from Ref.⁴⁰.

The interaction energies $U^*(t)$ and $U^+(t)$ are shown in Figure 9 for Rb in the $\Sigma_{1/2}$ -state in a), for the $\Pi_{1/2}$ -state in b), and for the $\Pi_{3/2}$ -state in c). Figure 9 d) shows the evolution following the sudden relaxation of Rb to the $\Pi_{1/2}$ -state at $t = 60$ ps. The prompt desorption of Rb in the $\Sigma_{1/2}$ and $\Pi_{1/2}$ -states is seen as a sudden drop of $U^*(t)$ near $t = 0$ followed by a slow rise towards zero due to long-range van der Waals attraction as Rb departs from the He droplet. Due to the purely attractive interaction of the Rb^+ ion with the He droplet, $U^+(t)$ monotonically rises to zero. The exciplex formation dynamics in the $\Pi_{3/2}$ -state is reflected by the irregular behavior of $U^*(t)$ and $U^+(t)$, eventually stabilizing at $t > 60$ ps at negative values, *i. e.* in a configuration where Rb is bound to the He droplet. Only when allowing for a sudden relaxation into the $\Pi_{1/2}$ -state at $t = 60$ ps, the RbHe exciplex receives a momentum “kick” and subsequently detaches from the He droplet, in spite of a rising $U^*(t)$. The asymptotic values of U^* and U^+ are then given by the binding energy of the free RbHe exciplex configuration. The fast oscillations at $t > 65$ ps indicate that RbHe keeps vibrating as it is ejected.

5 Discussion

Knowledge of the interaction energies $U^*(t)$ and $U^+(t)$ allows us to determine the electron binding energy $E_b(t) = U^+(t) - U^*(t)$ and to compare it with the experimental photoelectron spectra. Here, $U^*(t)$ and $U^+(t)$ are referenced to their asymptotic values, *i. e.* the binding energies of free Rb and Rb^+ , respectively. The resulting values of E_b are depicted as thick colored lines in Figure 10 in the range of delay times 0-100 ps. Compared to the experimental values, we note both matches and deviations. The TD-DFT values of E_b for the $\Pi_{1/2}$ -state (red line) converge within 100 ps to the value of the free Rb($5p_{1/2}$)-atom, as in the simulation Rb in that state detaches from the droplet. In contrast, the experimental values (blue symbols) are constant and below the atomic value because most of the atoms actually remain bound to the He droplet, see section 3.2.

The TD-DFT values for the $\Sigma_{1/2}$ -state (green line) quickly rise

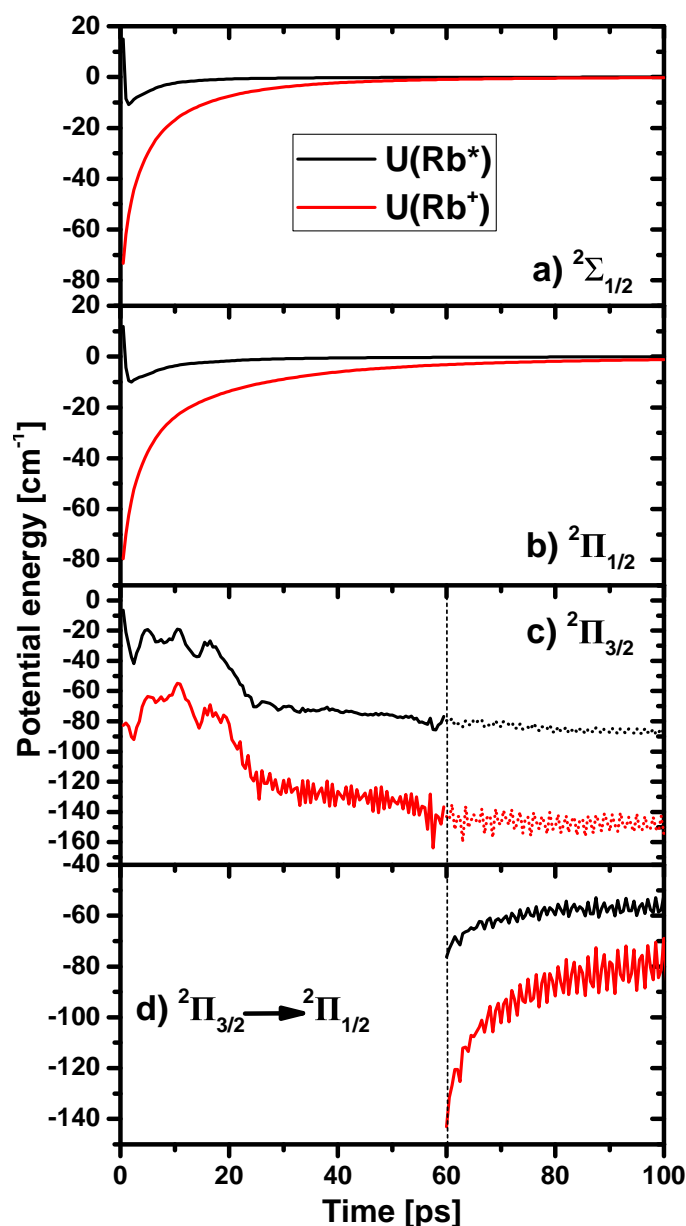


Figure 9 Simulated energies of the Rb-atom excited into various states interacting with the surrounding He distribution (black lines), and of the Rb⁺ ion for the same momentary geometry (red lines). In d), the excited state of Rb is suddenly switched from $\Pi_{3/2}$ to $\Pi_{1/2}$ to simulate the dynamics initiated by spin-relaxation.

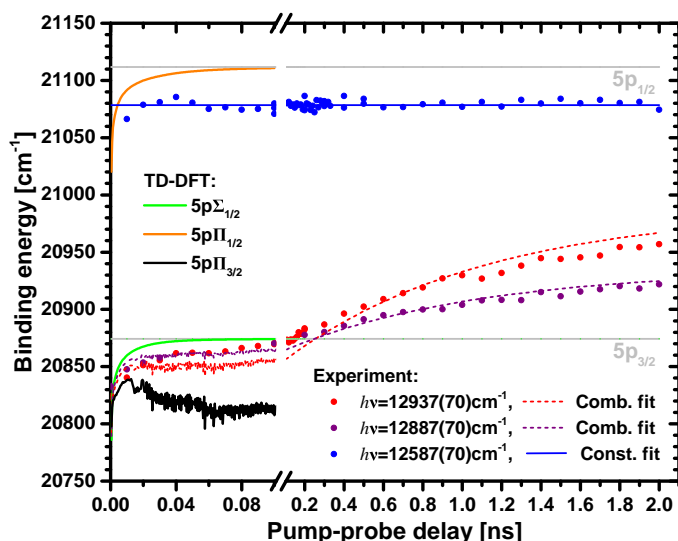


Figure 10 Comparison of experimental and simulated electron binding energies. Thick solid lines: TD-DFT results. Dashed lines: Combined TD-DFT and analytical model. Thin solid lines: Biexponential fits of the experimental data.

to $E_{5p_{3/2}}$ within a few tens of ps, again due to prompt desorption, yielding free Rb $5p_{3/2}$ atoms. The experimental values for excitation at 12,937 and 12,887 cm^{-1} (red and grey symbols) show a very similar increase in that time range. This supports our conclusion that the fast dynamics observed both in the photoelectron peak position and in the yield of photoions mainly results from prompt desorption of the $\Sigma_{1/2}$ -component of the excited state. In the experiment we found that the $[\text{RbHe}]^+$ ion signal associated with $\Pi_{3/2}$ -component of the excitation features a weak fast rising component as well [Figure 3 c)]. This we attribute to a finite rate of prompt desorption of Rb and RbHe in the $\Pi_{3/2}$ -state.

The TD-DFT curve for the $\Pi_{3/2}$ -state without relaxation (black line) drops in binding energy, at odds with the experiment. However, when $\Pi_{3/2} \rightarrow \Pi_{1/2}$ -relaxation is included, the simulated curve also rises, staying only slightly below the experimental values in the time range 20-100 ps. Thus, we achieve good agreement of our extended TD-DFT simulations with the experiment for the fast (tens of ps) desorption of the $\Sigma_{1/2}$ -state, and qualitative agreement with regard to the desorption of the $\Pi_{3/2}$ -state when allowing for spin-relaxation.

The lacking quantitative agreement is not surprising given the simplicity of our assumption – instantaneous spin-relaxation. Naturally, this relaxation process has its own time dependence. If we identify the latter with the observed slow variation of photoelectron spectra and ion yields, we can set up a more realistic, combined model. Hereby, we account for the populations $p_{\Sigma_{1/2}}$ in the $\Sigma_{1/2}$ -state and $p_{\Pi_{3/2}}$ in the $\Pi_{3/2}$ state, which are determined by the spectral profile of the laser $I_{\ell}(h\nu)$. The coefficients $p_{\Sigma_{1/2}, \Pi_{3/2}}$ are calculated from the state-selective absorption profiles $I_{\Sigma}(h\nu)$ and $I_{\Pi}(h\nu)$ using LeRoy's LEVEL program⁷⁵ based on the spin-orbit corrected pseudodiatomic potentials by Callegari and Ancilotto⁶⁵. In a second step, the absorption profiles are weighted with $I_{\ell}(h\nu)$ and integrated over $h\nu$, yielding $p_{\Pi_{3/2}} = 0.28$ for the center frequency $h\nu = 12,937 \text{ cm}^{-1}$ and

$p_{\Pi_{3/2}} = 0.52$ for $h\nu = 12,887 \text{ cm}^{-1}$.

The transient energy of the $\Pi_{3/2}$ -state, $E_{\Pi_{3/2}}(t)$, consists of a contribution of the binding energy $[U_{\Pi_{3/2} \rightarrow \Pi_{1/2}}^+ - U_{\Pi_{3/2} \rightarrow \Pi_{1/2}}^*]$ for the dynamics including relaxation to $\Pi_{1/2}$, and a contribution $[U_{\Pi_{3/2}}^+ - U_{\Pi_{3/2}}^*]$ for the $\Pi_{3/2}$ -state without relaxation. When assuming an exponential time dependence of the relaxation with a time constant τ , we get

$$E(t) = p_{\Sigma_{1/2}} \cdot [U_{\Sigma_{1/2}}^+ - U_{\Sigma_{1/2}}^*] + p_{\Pi_{3/2}} \cdot e^{-\ln 2 / \tau} \cdot [U_{\Pi_{3/2}}^+ - U_{\Pi_{3/2}}^*] \\ + p_{\Pi_{3/2}} \cdot (1 - e^{-\ln 2 / \tau}) \cdot [U_{\Pi_{3/2} \rightarrow \Pi_{1/2}}^+ - U_{\Pi_{3/2} \rightarrow \Pi_{1/2}}^*].$$

Here, $U^*(t)$ and $U^+(t)$ are extrapolated for long times $t > 200$ ps by constants for the $\Sigma_{1/2}$ and $\Pi_{3/2}$ -states and by an exponential function for the $\Pi_{3/2} \rightarrow \Pi_{1/2}$ case. For simplicity, we neglect the 60 ps time delay between excitation and relaxation which is short compared to the full relaxation dynamics.

If we assign to τ the experimental value of the slow time constant of the fit of photoelectron energies, $\tau = \tau_2^e$, we obtain the dashed lines in Figure 10, which nicely match the experimental data. Thus, we identify the slow variations of ion and electron signals spanning hundreds of ps to He-induced spin-relaxation, which proceeds on that time scale and causes the desorption of RbHe exciplexes. The fact that the Rb^+ signal associated mainly with $\Sigma_{1/2}$ -excitation features a weak slowly rising component as well [Figure 3 c) and d)], we take as an indication that spin-relaxation also causes the desorption of neat $\text{Rb}(5p_{1/2})$ -atoms to some extent.

6 Conclusion

In summary, we have presented a detailed study of the formation and desorption dynamics of RbHe exciplexes initiated by laser excitation of Rb atoms attached to He nanodroplets. Experimentally, the two-color femtosecond pump-probe photoionization scheme allows us to selectively probe the dynamics of the lowest three excited states of the Rb-He droplet complex. Both photoion and photoelectron signals feature pump-probe dynamics proceeding on two distinct time scales (~ 30 and 700 ps). By comparing with time-dependent DFT simulations, complemented by a spin-relaxation mechanism, we conclude that the fast dynamics is due to prompt desorption of Rb atoms when exciting the $\Sigma_{1/2}$ -state. The slow desorption of RbHe exciplexes is induced by $\Pi_{3/2} \rightarrow \Pi_{1/2}$ spin-relaxation. By analyzing the rearrangement of the He surrounding the Rb atom in the $\Pi_{3/2}$ -state, we infer a formation time of the RbHe exciplex ranging between 20 and 50 ps. When exciting the lowest state of the Rb-He droplet complex, $\Pi_{1/2}$, we find that a small fraction of Rb atoms desorbs as free atoms, as predicted by the DFT simulation, whereas the larger fraction Rb atoms remains bound to the He droplets.

While this work represents in our opinion the most complete investigation of the real-time dynamics of an alkali metal-He exciplex, still some uncertainties remain. In the experiment, a better reconcilability of electron and ion signals may be achieved by detecting electrons and ions in coincidence^{71,76}. Furthermore, extending such studies to other types of dopant species which are solvated more deeply inside He droplets (e. g. alkaline earth met-

als, transition metals) would give further insight into the mechanisms of desolvation and ejection of excited impurity atoms out of He nanodroplets^{18,20,21,77}.

On the theory side, a more complete description of the couplings between electronic states and the configurational degrees of freedom in such excited complexes induced by the He droplet environment would be highly desirable^{3,4}. In a recent advance, electronic relaxation of Ba^+ ions in He nanodroplets, based on a diabaticization of the He- Ba^+ ground and excited electronic states interaction potentials⁵, has been proposed as a mechanism for ejecting Ba^+ and Ba^+He_n off He droplets. These mechanisms for spin-relaxation and inter-electronic state relaxation have to be confirmed by real-time dynamics studies.

6.0.0.1 Acknowledgements The authors would like to thank Marcel Drabbels for useful exchanges. Financial support by the Deutsche Forschungsgemeinschaft (MU 2347/6-1 and IRTG 2079) is gratefully acknowledged. This work has been performed under Grant No. FIS2017-87801-P from DGI, Spain. M. B. thanks the Université Fédérale Toulouse Midi-Pyrénées for financial support throughout the “Chaires d’Attractivité 2014” Programme IM-DYNHE. The dynamics simulations presented in this work have been carried out thanks to the HPC resources of CALMIP supercomputing center (Grant P1039).

References

- 1 C. George, M. Ammann, B. D’Anna, D. J. Donaldson and S. A. Nizkorodov, *Chem. Rev.*, 2015, **115**, 4218–4258.
- 2 J. Schneider, D. Bahnemann, J. Ye, G. L. Puma and D. D. Dionysiou, *Photocatalysis: Fundamentals and Perspectives*, The Royal Society of Chemistry, Cambridge CB4 0WF, UK, 2016.
- 3 K. D. Closser, O. Gessner and M. Head-Gordon, *J. Chem. Phys.*, 2014, **140**, 134306.
- 4 A. Masson, M.-C. Heitz, J.-M. Mestdagh, M.-A. Gaveau, L. Poisson and F. Spiegelman, *Phys. Rev. Lett.*, 2014, **113**, 123005.
- 5 P. Vindel-Zandbergen, M. Barranco, F. Cargnoni, M. Drabbels, M. Pi and N. Halberstadt, *Helium-induced electronic transitions in photo-excited $\text{Ba}^+\text{-He}_n$ exciplexes*, submitted, 2018.
- 6 J. P. Toennies and A. F. Vilesov, *Angew. Chem. Int. Ed.*, 2004, **43**, 2622.
- 7 F. Stienkemeier and K. Lehmann, *J. Phys. B*, 2006, **39**, R127.
- 8 F. Ancilotto, G. DeToffol and F. Toigo, *Phys. Rev. B*, 1995, **52**, 16125–16129.
- 9 F. Stienkemeier, J. Higgins, C. Callegari, S. I. Kanorsky, W. E. Ernst and G. Scoles, *Z. Phys. D*, 1996, **38**, 253–263.
- 10 M. Barranco, R. Guardiola, S. Hernández, R. Mayol, J. Navarro and M. Pi, *J. Low Temp. Phys.*, 2006, **142**, 1–81.
- 11 C. Stark and V. V. Kresin, *Phys. Rev. B*, 2010, **81**, 085401.
- 12 L. An der Lan, P. Bartl, C. Leidlmair, H. Schöbel, R. Jochum, S. Denifl, T. D. Märk, A. M. Ellis and P. Scheier, *J. Chem. Phys.*, 2011, **135**, 044309.
- 13 L. An der Lan, P. Bartl, C. Leidlmair, H. Schöbel, S. Denifl, T. D. Märk, A. M. Ellis and P. Scheier, *Phys. Rev. B*, 2012, **85**, 115414.

- 14 Höller, Johannes, Krotscheck, Eckhard and Zillich, Robert E., *Eur. Phys. J. D*, 2015, **69**, 198.
- 15 F. Calvo, *Phys. Rev. B*, 2017, **95**, 035429.
- 16 M. Mudrich and F. Stienkemeier, *Int. Rev. Phys. Chem.*, 2014, **33**, 301–339.
- 17 F. Ancilotto, M. Barranco, F. Coppens, J. Eloranta, N. Halberstadt, A. Hernando, D. Mateo and M. Pi, *Int. Rev. Phys. Chem.*, 2017, **36**, 621–707.
- 18 E. Loginov and M. Drabbels, *J. Phys. Chem. A*, 2007, **111**, 7504–7515.
- 19 L. Fechner, B. Grüner, A. Sieg, C. Callegari, F. Ancilotto, F. Stienkemeier and M. Mudrich, *Phys. Chem. Chem. Phys.*, 2012, **14**, 3843.
- 20 A. Kautsch, M. Koch and W. E. Ernst, *J. Phys. Chem. A*, 2013, **117**, 9621–9625.
- 21 F. Lindebner, A. Kautsch, M. Koch and W. E. Ernst, *Int. J. Mass Spectrom.*, 2014, **365–366**, 255–259.
- 22 M. Koch, G. Auböck, C. Callegari and W. E. Ernst, *Phys. Rev. Lett.*, 2009, **103**, 035302.
- 23 S. Smolarek, N. B. Brauer, W. J. Buma and M. Drabbels, *J. Am. Chem. Soc.*, 2010, **132**, 14086–14091.
- 24 A. Hernando, M. Barranco, M. Pi, E. Loginov, M. Langlet and M. Drabbels, *Phys. Chem. Chem. Phys.*, 2012, **14**, 3996–4010.
- 25 D. Mateo, A. Hernando, M. Barranco, E. Loginov, M. Drabbels and M. Pi, *Phys. Chem. Chem. Phys.*, 2013, **15**, 18388–18400.
- 26 J. von Vangerow, A. Sieg, F. Stienkemeier, M. Mudrich, A. Leal, D. Mateo, A. Hernando, M. Barranco and M. Pi, *J. Phys. Chem. A*, 2014, **118**, 6604–6614.
- 27 J. von Vangerow, O. John, F. Stienkemeier and M. Mudrich, *J. Chem. Phys.*, 2015, **143**, 034302.
- 28 A. Sieg, J. von Vangerow, F. Stienkemeier, O. Dulieu and M. Mudrich, *J. Phys. Chem. A*, 2016, **120**, 7641–7649.
- 29 J. von Vangerow, F. Coppens, A. Leal, M. Pi, M. Barranco, N. Halberstadt, F. Stienkemeier and M. Mudrich, *J. Phys. Chem. Lett.*, 2017, **8**, 307–312.
- 30 A. Przystawik, S. Göde, T. Döppner, J. Tiggesbäumker and K.-H. Meiwes-Broer, *Phys. Rev. A*, 2008, **78**, 021202.
- 31 S. Müller, S. Krapf, T. Kosłowski, M. Mudrich and F. Stienkemeier, *Phys. Rev. Lett.*, 2009, **102**, 183401.
- 32 A. Kautsch, M. Koch and W. E. Ernst, *Phys. Chem. Chem. Phys.*, 2015, **17**, 12310–12316.
- 33 J. Reho, J. Higgins, C. Callegari, K. K. Lehmann and G. Scoles, *J. Chem. Phys.*, 2000, **113**, 9694–9701.
- 34 F. R. Brühl, R. A. Trasca and W. E. Ernst, *J. Chem. Phys.*, 2001, **115**, 10220–10224.
- 35 C. P. Schulz, P. Claas and F. Stienkemeier, *Phys. Rev. Lett.*, 2001, **87**, 153401.
- 36 G. Droppelmann, O. Bünermann, C. P. Schulz and F. Stienkemeier, *Phys. Rev. Lett.*, 2004, **93**, 0233402.
- 37 M. Mudrich, G. Droppelmann, P. Claas, C. Schulz and F. Stienkemeier, *Phys. Rev. Lett.*, 2008, **100**, 023401.
- 38 S. Müller, M. Mudrich and F. Stienkemeier, *J. Chem. Phys.*, 2009, **131**, 044319.
- 39 M. Theisen, F. Lackner and W. E. Ernst, *Phys. Chem. Chem. Phys.*, 2010, **12**, 14861–14863.
- 40 A. Leal, D. Mateo, A. Hernando, M. Pi, M. Barranco, A. Ponti, F. Cargnoni and M. Drabbels, *Phys. Rev. B*, 2014, **90**, 224518.
- 41 E. Loginov, A. Hernando, J. A. Beswick, N. Halberstadt and M. Drabbels, *J. Phys. Chem. A*, 2015, **119**, 6033–6044.
- 42 M. Kuhn, M. Renzler, J. Postler, S. Ralser, S. Spieler, M. Simpson, H. Linnartz, A. G. G. M. Tielens, J. Cami, A. Mau-racher, Y. Wang, M. Alcamí, F. Martín, M. K. Beyer, R. Wester, A. Lindinger and P. Scheier, *Nat. Comm.*, 2016, **7**, 13550.
- 43 N. B. Brauer, S. Smolarek, E. Loginov, D. Mateo, A. Hernando, M. Pi, M. Barranco, W. J. Buma and M. Drabbels, *Phys. Rev. Lett.*, 2013, **111**, 153002.
- 44 M. Koch, A. Kautsch, F. Lackner and W. E. Ernst, *J. Phys. Chem. A*, 2014, **118**, 8373–8379.
- 45 Y. Seki, T. Takayanagi and M. Shiga, *Phys. Chem. Chem. Phys.*, 2017, **19**, 13798–13806.
- 46 G. Auböck, J. Nagl, C. Callegari and W. E. Ernst, *Phys. Rev. Lett.*, 2008, **101**, 035301.
- 47 M. Theisen, F. Lackner and W. E. Ernst, *J. Phys. Chem. A*, 2011, **115**, 7005–7009.
- 48 T. Takayanagi and M. Shiga, *Phys. Chem. Chem. Phys.*, 2004, **6**, 3241.
- 49 M. Leino, A. Viel and R. E. Zillich, *J. Chem. Phys.*, 2011, **134**, 024316.
- 50 C. Giese, T. Mullins, B. Grüner, M. Weidemüller, F. Stienkemeier and M. Mudrich, *J. Chem. Phys.*, 2012, **137**, 244307.
- 51 S. H. Patil, *J. Chem. Phys.*, 1991, **94**, 8089–8095.
- 52 J. Pascale, *Phys. Rev. A*, 1983, **28**, 632–644.
- 53 F. Ancilotto, M. Barranco, F. Caupin, R. Mayol and M. Pi, *Phys. Rev. B*, 2005, **72**, 214522.
- 54 M. Pi, F. Ancilotto, F. Coppens, N. Halberstadt, A. Hernando, A. Leal, D. Mateo, R. Mayol and M. Barranco, *⁴He-DFT BCN-TLS: A Computer Package for Simulating Structural Properties and Dynamics of Doped Liquid Helium-4 Systems*. <https://github.com/bcntls2016/>.
- 55 D. Mateo, A. Hernando, M. Barranco, R. Mayol and M. Pi, *Phys. Rev. B*, 2011, **83**, 174505.
- 56 A. Hernando, M. Barranco, R. Mayol, M. Pi and M. Krośnicki, *Phys. Rev. B*, 2008, **77**, 024513.
- 57 O. Bünermann, G. Droppelmann, A. Hernando, R. Mayol and F. Stienkemeier, *J. Phys. Chem. A*, 2007, **111**, 12684.
- 58 K. Hirano, K. Enomoto, M. Kumakura, Y. Takahashi and T. Yabuzaki, *Phys. Rev. A*, 2003, **68**, 012722.
- 59 A. T. J. B. Eppink and D. H. Parker, *Rev. Sci. Instrum.*, 1997, **68**, 3477.
- 60 A. Wituschek, J. von Vangerow, J. Grzesiak, F. Stienkemeier and M. Mudrich, *Rev. Sci. Instrum.*, 2016, **87**, 083105.
- 61 G. A. Garcia, L. Nahon and I. Powis, *Rev. Sci. Instrum.*, 2004, **75**, 4989–4996.
- 62 B. Dick, *Phys. Chem. Chem. Phys.*, 2014, **16**, 570–580.
- 63 A. Braun and M. Drabbels, *J. Chem. Phys.*, 2007, **127**, 114303.
- 64 G. S. Mudholkar and A. D. Hutson, *J. Stat. Plan. Inference*, 2000, **83**, 291–309.

- 65 C. Callegari and F. Ancilotto, *J. Phys. Chem. A*, 2011, **115**, 6789–6796.
- 66 R. N. Zare, *Mol. Photochem.*, 1972, **44**, 1.
- 67 M. Theisen, F. Lackner, G. Krois and W. E. Ernst, *J. Phys. Chem. Lett.*, 2011, **2**, 2778–2782.
- 68 E. Loginov, D. Rossi and M. Drabbels, *Phys. Rev. Lett.*, 2005, **95**, 163401.
- 69 D. S. Peterka, J. H. Kim, C. C. Wang and D. M. Neumark, *J. Phys. Chem. B*, 2006, **110**, 19945–19955.
- 70 C. C. Wang, O. Kornilov, O. Gessner, J. H. Kim, D. S. Peterka and D. M. Neumark, *J. Phys. Chem. A*, 2008, **112**, 9356.
- 71 D. Buchta, S. R. Krishnan, N. B. Brauer, M. Drabbels, P. O’Keeffe, M. Devetta, M. Di Fraia, C. Callegari, R. Richter, M. Coreno, K. C. Prince, F. Stienkemeier, R. Moshhammer and M. Mudrich, *J. Phys. Chem. A*, 2013, **117**, 4394–4403.
- 72 M. Leino, A. Viel and R. E. Zillich, *J. Chem. Phys.*, 2008, **129**, 184308.
- 73 E. Loginov and M. Drabbels, *J. Phys. Chem. A*, 2014, **118**, 2738–2748.
- 74 L. Krause, in *Adv. Chem. Phys.*, edited by J. W. McGowan (Wiley, New York), 1975.
- 75 R. LeRoy, *Chemical Physics Research Report*, University of Waterloo, CP-555, 1995, 1995.
- 76 A. C. LaForge, V. Stumpf, K. Gokhberg, J. von Vangerow, F. Stienkemeier, N. V. Kryzhevoi, P. O’Keeffe, A. Ciavardini, S. R. Krishnan, M. Coreno, K. C. Prince, R. Richter, R. Moshhammer, T. Pfeifer, L. S. Cederbaum and M. Mudrich, *Phys. Rev. Lett.*, 2016, **116**, 203001.
- 77 E. Loginov and M. Drabbels, *J. Chem. Phys.*, 2012, **136**, 154302.